Journal of Alloys and Compounds 527 (2012) 53–65

Contents lists available at SciVerse ScienceDirect

Journal of Alloys and Compounds

journal homepage: www.elsevier.com/locate/jallcom

Quantitative crystallographic analysis of as-fabricated full size U–Mo/Al(Si) nuclear fuel plates

H. Palancher[a,*], A. Bonnin[a,b], V. Honkimäki[b], T. Buslaps[b], M. Grasse[c], B. Stepnik[c], T. Zweifel[a,d]

[a] CEA, DEN, DEC, F-13108 St Paul Lez Durance Cedex, France
[b] ESRF, 6, rue J. Horowitz, 38500 Grenoble Cedex, France
[c] AREVA-CERCA, Les Berauds, B.P. 1114, 26104 Romans Cedex, France
[d] FRM II, Technische Universität München, Lichtenbergstr. 1, 85747 Garching, Germany

ARTICLE INFO

Article history:
Received 3 October 2011
Received in revised form 30 January 2012
Accepted 1 February 2012
Available online xxx

Keywords:
High energy XRD
Rietveld method
U–Mo alloy
Non proliferation

ABSTRACT

The optimisation of high density metallic U–Mo/Al(Si) nuclear fuels, developed for use in high neutron flux research reactor without proliferation issues, requires an excellent control of the manufacturing conditions for getting a full benefit of Si powder additions. Eleven full size plates (from the IRIS and E-FUTURE experimental programs) have been analysed by diffraction using synchrotron high energy X-rays. For the first time, both the levels of the γU–Mo phase destabilisation in the U–Mo particle and characteristics (size and composition) of the Si rich protective layers around these particles have been quantified at a macroscopic scale. These results enable to evaluate the influence of the different parameters implied in the manufacturing process and could also provide solutions for producing enhanced fuels.

1. Introduction

A worldwide program encourages the development of low (below 20%) ^{235}U enriched fuels in order to convert research reactors cores (materials testing reactors, neutron sources. . .) currently working with highly enriched (up to 93%) U_3Si_2, UAl_x or U_3O_8 fuels. For the most powerful cores, U-*x*Mo[1] alloys appear as the only fuel material that could enable their conversion without decreasing their performance (i.e. the neutron flux).

This material has been selected because of its high uranium density (more than 15 gU cm^{-3}) that compensates partly the decrease in ^{235}U enrichment and because of its cubic crystal structure that ensures isotropic (and thus limited) swelling under irradiation. Note that Mo is required for stabilisation at room temperature of the high temperature (γ) cubic phase of metallic uranium. Indeed the U phases stable at lower temperature, i.e. αU (from room temperature up to 667 °C) [1] and βU (between 667 and 773 °C) [2] are orthorhombic and tetragonal, respectively.

U–Mo fuel elements usually consist of fissile particles (either produced by a grinding or an atomisation process) dispersed in an Al matrix. However the in-pile behaviour of these fuels has been for a long time limited by the growth of an intermetallic interaction layer (IL) at the interfaces between U–Mo and the matrix [3]. Indeed this IL exhibits poor gaseous fission products retention, resulting in an accumulation (large interconnected bubbles) of fission gas at the interface between the interaction layer and the matrix [4–6].

A solution for optimising this in-pile behaviour has been obtained by adding some Si to the Al matrix [7–9]. If an U–Mo/Al interaction layer may still grow under in-pile irradiation, the IL thickness is strongly reduced and large pores appear at much higher burn-up [8].

It has been shown that a pre-existing Si rich diffusion layer (SiRDL) developed before irradiation (during the fuel plate manufacturing by hot-rolling) could have a beneficial role under irradiation. However manufacturing conditions still have to be optimised especially to improve the features of this SiRDL and the composition of the U–Mo particles. Two parameters are known to modify the characteristics of the SiRDL: Si weight fraction in the Al matrix and a combination of temperature (between 400 and 600 °C) and duration (a few hours) of the thermal treatments performed during the manufacturing process of these fuel plates. A methodology needs however to be defined to provide (i) a robust value for the SiRDL thickness averaged over a large number of U–Mo particles, i.e. over a large meat volume, (ii) an accurate crystallographic composition of these U–Mo/AlSi shells since few data are available in the literature in the [425; 475 °C] temperature range [10,11], (iii) the Si repartition in the meat (located either in precipitates in the matrix or in the SiRDL).

* Corresponding author. Tel.: +33 442 257 555, fax: +33 442 253 285.
E-mail address: herve.palancher@cea.fr (H. Palancher).

[1] In this notation, *x* stands for the Mo weight fraction in UMo_x alloys. For example 8 wt% corresponds to about 15 at%.

0925-8388/$ – see front matter © 2012 Elsevier B.V. All rights reserved.
doi:10.1016/j.jallcom.2012.02.010

Table 1
Characteristics of the 11 U–Mo/Al analysed nuclear fuel plates.

	U–Mo powders			Matrix				Cladding	Post manufacturing thermal treatment	
	Fabrication type	Mo content (wt%)	U loading (gU cm^{-3})	Fraction in the core (wt%)	Si fraction in (wt%)		AlSi manufacturing process	Al type	Temperature (°C)	Time (h)
					Matrix	Meat				
IRISTUM_0%Si	Ground	8.1	<8.0	9.9	0			AlFeNi	425	2
IRISTUM_2.1%Si	Ground	8.1	<8.0	9.9	2.1	0.20	Alloy	AlFeNi	425	2
IRIS1_0%Si	Ground	7.6	7.9–8.3	9.5	0			AG3	425	2
IRIS3_0.3%Si	Atomised	7.2	7.8–8.0	13.4	0.3			AG3	425	2
IRIS3_2.1%Si	Atomised	7.2	7.8–8.0	13.4	2.1	0.27	Alloy	AG3	425	2
IRIS4_0%Si	Atomised/oxidised	7.3	7.9	13.1	0			AlFeNi	425	2
IRIS4_2.1%Si	Atomised/oxidised	7.3	7.9	13.4	2.1	0.27	Alloy	AlFeNi	425	2
EF4112_4%Si	Atomised	7.4	~8.0	12.9	4	0.49	Mixing	AlFeNi	425	2
EF6101_6%Si	Atomised	7.4	~8.0	12.9	6	0.73	Mixing	AG3	425	2
EF4201_4%Si	Atomised	7.4	~8.0	12.9	4	0.49	Mixing	AG3	475	2
EF6311_6%Si	Atomised	7.4	~8.0	12.9	6	0.73	Mixing	AlFeNi	475	4

The standard deviations associated with the Mo weight fraction in the U–Mo particles and the matrix (Al or AlSi) weight fraction in the meat are estimated to be 0.3% and below 0.1%, respectively.

It is well known that under standard fabrication conditions the metastable γU–Mo phase will partly decompose in αU and either a Mo enriched γU–Mo phase or U_2Mo [12]. A certain level of destabilisation is therefore expected when investigating the as-fabricated fuel plates. Moreover depending on the annealing conditions (temperature and duration), the destabilisation levels are expected to be different. Note that the identification of U_2Mo by XRD is quite difficult because of the small grain size of this phase.

To better characterise the specificities of U–Mo/AlSi fuel plates, a methodology based on macroscopic, volume, quantitative and accurate X-ray diffraction (XRD) measurements has thus been developed. It has been applied to a unique set of fuel plates in the as-fabricated state: 11 plates manufactured and irradiated within the IRIS, IRIS-TUM (see [13–15] and reference therein) and E-FUTURE (see [16,17]) research programs. Only the IRIS2 fresh fuel plate was not available for analysis during the measurement period.

In this article after having specified both the fuel plate composition and manufacturing process, XRD measurements will be presented. Calculations for evaluating the γU–Mo phase destabilisation and the average SiRDL thickness will then be justified. In a next step the results obtained for each analysed fuel plate will be discussed opening the way towards a description of the Si behaviour during the manufacturing process. Finally an optimisation of the U–Mo/Al(Si) fuel plate fabrication conditions will be proposed.

2. Experimental methods

2.1. Fuel plate manufacturing

The IRIS and E-FUTURE nuclear fuel plates have been produced by AREVA-CERCA.

Atomised powders were provided by the Korean Atomic Energy Research Institute (KAERI) while ground U–Mo particles were manufactured by arc melting followed by a grinding step at AREVA-CERCA. The Mo content is usually between 7 and 10 wt% (i.e. 13.6–21.6 at%) in the U–Mo alloy. Depending on the production process, U–Mo particles exhibit different shapes (but also microstructures): they are spherical if obtained by atomisation or irregular shaped when manufactured by grinding. Their typical size (diameter) ranges from a few micrometers up to 125 μm. Note that in the IRIS4_0%Si and IRIS4_2.1%Si nuclear fuel plates the U–Mo atomised powders underwent an oxidation process.

These powders were then mixed with pure Al (A5 type) or AlSi powders with a weight ratio of about 12/88 wt% (for AlSi and U–Mo, respectively) to obtain a high uranium loading. These AlSi powders, labelled in the following the "matrix", are produced either via alloying or by mixing.

After compaction, this mixture (referred to as the meat) is placed in an Al frame and then pressed between two Al sheets which will serve as a cladding. The material used for the frame is AG3NE [18] whereas the alloys for the cladding are either AG3NE or AlFeNi [19].

Plates are heated and then rolled until their thickness complies with the specifications. At the end of this process, the whole fuel plate is about 1.3 mm thick, each Al sheet (cladding) less than 0.4 mm and the meat slightly more than 0.5 mm. The as such produced fuel plates are then annealed for another 2–4 h at either 425 or 475 °C. This post-manufacturing thermal treatment referred to as blister test in the literature is performed to check that the meat and the cladding are well in contact.

For each of the 11 fuel plates of interest, Table 1 gives the precise values of the Mo content inside the U–Mo particles (ion chromatography/inductively coupled plasma (ICP) measurements), the uranium loading, the AlSi and U–Mo powder manufacturing process as well as their weight ratios in the meat, the silicon concentration in the matrix and in the meat, and the alloy used for cladding. Furthermore the post-manufacturing thermal treatment characteristics (temperature and anneal time) are mentioned.

2.2. Sample preparation

For each fuel plate to test in-pile, an additional spare item has been produced (which will be referred to as fresh fuel plate). A square of $10 \times 10\,mm^2$ has been cut out of the fresh fuel plate at a location chosen far enough from the interface between the meat and the frame: it has been shown that the fuel particles are often oxidised in this area [20].

Next the cladding material has been removed on both sides by conventional mechanical polishing techniques. In other words, the current work focuses on the analysis of the meat.

2.3. XRD mapping at 87 keV in transmission mode

Measurements have been performed at the ID15B beamline (ESRF) in transmission mode using a 87 keV X-ray beam. Its footprint on the sample was set to $0.3 \times 0.3\,mm^2$. For each sample 200 images (counting time set as 40 s per image) were collected using a Pixium flat panel bi-dimensional detector.

The XRD images relating to the same plate have been averaged, the result being converted into a 1D pattern. For that purpose, the Fit2D software has been used [21]. This conversion from an averaged image to a pattern is illustrated in Fig. 1 with the data measured on the EF6101_6%Si plate. Fig. 2 shows a comparison between the patterns collected on each fuel plate.

3. XRD data analysis: description, interests and limits

3.1. Rietveld refinement

Diffraction data have been analysed with the FullProf software package using the Rietveld method [22,23]. A preliminary step of this fitting procedure has been dedicated to the analysis of the γU–Mo complex peak shape: best modelling is obtained using two γU–Mo phases with different lattice parameters. Such occurrence of two γU–Mo phases in atomised UMo powders has already been reported elsewhere [24]. The γU–Mo phase with the largest cell parameter is written γU–Mo-a and the one with the smallest γU–Mo-b.

At least nine phases have been included in the refinement: five phases (αU, γU–Mo-a, γU–Mo-b, U_2Mo, UC) describing the U–Mo

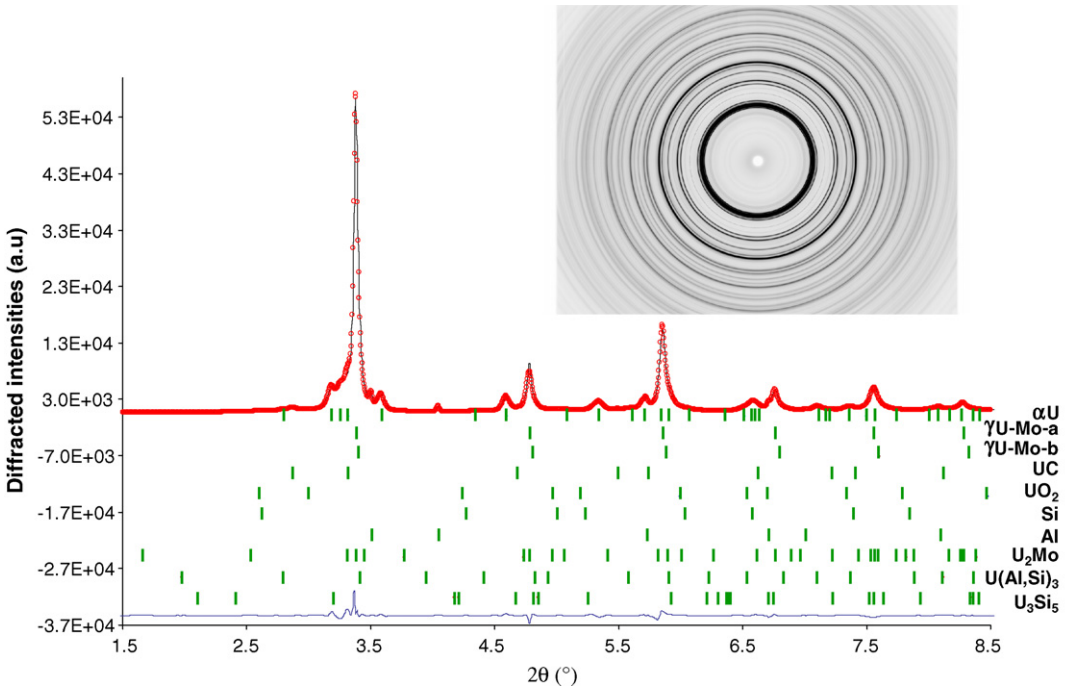

Fig. 1. High energy X-ray diffraction images (*inset*) and patterns measured (red circles) on EF6101_6%Si. Black and blue lines indicate the associated calculated and difference patterns, respectively. (For interpretation of the references to colour in this figure legend, the reader is referred to the web version of the article.)

particles themselves, three phases describing their protective shells ($U(Al,Si)_3$, U_3Si_5, UO_2) and two for the matrix (Al and Si). In certain cases, additional phases were considered in the refinement: UN, U_2N_{3+x}, UAl_2 or UAl_3. Much more details on that point will be given in following sections (i.e. 5, 6). The 2θ angle position of each Bragg line in 10 of these phases can be seen in Fig. 1. The calculated lattice constants of the αU, γU–Mo-a and γU–Mo-b phases for each sample are indicated in Table 2.

To improve the fitting quality, the background was described by about 40 points rather than by a mathematical function. This "difficult background" is mainly due to phonon excitations but the presence of small amounts of ill-ordered phases can not be excluded.

In the last step of the refinement, only the scale factors were left free (all other parameters were kept fixed). The obtained weight fractions for each crystallographic phase are indicated in Table 3. These values (written W_l) have been determined from the refined scale factors S_l using both the complete unit-cell mass (M_l), the number of formula units per unit cell (Z_l) and the unit-cell volume (V_l) of the l phase:

$$W_l = \frac{S_l Z_l M_l V_l / t_l}{\sum_k S_k Z_k M_k V_k / t_k}$$

Brindley factors (t_l in the last equation) equal to 1 for each phase of a given U–Mo/Al fuel plate measured by diffraction with high energy X-rays (87 keV) [25]. This is not the case for XRD characterisations using lower energies (8 keV for example) [25].

Note that the presence of Mo elements in the γU–Mo structure has been taken into account for determining the associated unit-cell mass ($M_{\gamma U-Mo}$). This was not the case in our previous works and may explain slight differences in the refined weight fractions for this phase [25,26].

The quality of the obtained fit can be seen in both Table 4 where the final agreement factors (R_p, R_{wp}, R_{exp}) are reported and in Fig. 2. This figure shows a comparison between measured and calculated patterns over the whole measured angular range for the 11 fuel plates of interest. For clarity three zooms are also presented in Fig. 3, Fig. 4, Fig. 5 for limited 2θ ranges ([1.5; 2.2], [2.4; 3.1], [3.1; 3.7]).

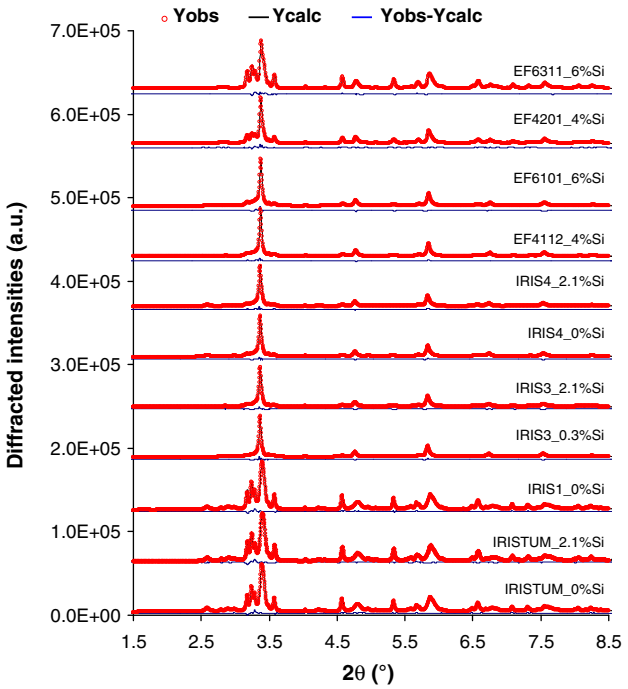

Fig. 2. High energy X-ray diffraction patterns measured (red circles) on 11 fuel plates. Black and blue lines indicate the associated calculated and difference patterns, respectively. (For interpretation of the references to colour in this figure legend, the reader is referred to the web version of the article.)

3.2. Matrix weight fractions

In Fig. 6 the Al weight fractions communicated by the manufacturer and those obtained through the above detailed XRD

Table 2
Influence of the U–Mo particle microstructure and post-manufacturing thermal treatment conditions on the measured lattice constants and the Mo content of three phases (γU–Mo-a, γU–Mo-b, αU) and of the U–Mo particles.

	Post manufacturing thermal treatment	U–Mo powder fabrication method	γU–Mo-a		γU–Mo-b		αU					Mo fraction in U–Mo particles (wt%)
			a_0	Mo fraction (wt%)	a_0	Mo fraction (wt%)	a	b	c	Mo fraction (wt%)	Crystal structure	
IRISTUM_0%Si	425 °C—2 h	Ground	3.412	10.3	3.387	14.5	2.860	5.844	4.964	–	α′U	8.7
IRISTUM_2.1%Si			3.412	10.3	3.387	14.5	2.860	5.842	4.965	–	α′U	8.5
IRIS1_0%Si			3.409	10.8	3.381	15.5	2.859	5.843	4.964	–	α′U	8.7
Average			*3.411*	*10.5*	*3.385*	*14.8*	*2.859*	*5.843*	*4.964*	–	*α′U*	*8.6*
IRIS3_0.3%Si	425 °C—2 h	Atomised	3.428	7.9	3.411	10.5	2.873	5.850	4.930	1.1	α″U	7.0
IRIS3_2.1%Si			3.429	7.7	3.411	10.4	2.873	5.846	4.932	1.8	α″U	6.8
IRIS4_0%Si			3.429	7.8	3.410	10.6	2.873	5.846	4.934	1.8	α″U	6.9
IRIS4_2.1%Si			3.43	7.7	3.412	10.3	2.873	5.850	4.935	2.2	α″U	6.8
EF4112_4%Si			3.428	7.9	3.414	10.0	2.872	5.850	4.937	2.7	α″U	6.9
EF6101_6%Si			3.427	8.0	3.410	10.6	2.872	5.848	4.941	2.7	α″U	6.8
Average			*3.429*	*7.8*	*3.412*	*10.4*	*2.872*	*5.848*	*4.935*	–	*α″U*	*6.9*
EF4201_4%Si	475 °C—2 h	Atomised	3.426	8.3	3.396	13.0	2.868	5.844	4.957	1.4	α″U	7.0
EF6311_6%Si	475 °C—4 h	Atomised	3.424	8.5	3.394	13.2	2.867	5.844	4.962	0.4	α′U	7.3

The errors associated with the lattice constant determination is estimated to below ±0.002 Å.

Table 3
Crystallographic composition of the 11 full size plates given by the Rietveld analysis of the diffraction data collected with a high energy X-ray beam. Values are given in wt%.

	U–Mo particle core					Protective layer (outer shell)					Matrix		Impurities
	αU	U_2Mo	γU–Mo-a	γU–Mo-b	UC	UN	U_2N_{3+x}	UO_2	$U(Al,Si)_3$	U_3Si_5	Al	Si	UAl_x
IRISTUM_0%Si	32.9 ± 0.1	8.3 ± 0.2	5.7 ± 0.1	35.7 ± 0.2	–	3.5 ± 0.1	–	4.8 ± 0.1	–	0.1*	9.2 ± 0.2	–	0.2*
IRISTUM_2.1%Si	31.9 ± 0.1	6.1 ± 0.2	8.8 ± 0.1	33.7 ± 0.2	–	2.9 ± 0.1	–	6.2 ± 0.1	0.2*	1.2*	9.3 ± 0.2	0*	0.1*
IRIS1_0%Si	31.1 ± 0.1	8.2 ± 0.2	13.5 ± 0.1	27.1 ± 0.2	–	3.4 ± 0.1	–	4.9 ± 0.1	–	0.1*	10.8 ± 0.2	–	0.2*
IRIS3_0.3%Si	13.6 ± 0.1	1.4*	61.3 ± 0.3	8.9 ± 0.2	1.1 ± 0	–	–	0.3*	–	–	13.4 ± 0.3	–	–
IRIS3_2.1%Si	17.7 ± 0.1	1.8 ± 0.2	50.2 ± 0.3	15.1 ± 0.2	0.8 ± 0	–	–	0.7 ± 0.1	0.1*	0.4	12.4 ± 0.3	0*	–
IRIS4_0%Si	17 ± 0.1	3.2*	44.7 ± 0.2	13.4 ± 0.2	0.8 ± 0	–	1.7 ± 0.1	6.2 ± 0.1	–	–	13.1 ± 0.3	–	–
IRIS4_2.1%Si	16.2 ± 0.1	2.4 ± 0.2	44.3 ± 0.3	14.5 ± 0.2	0.6 ± 0	–	1.0 ± 0.1	6.3 ± 0.1	0*	0.3*	14.4 ± 0.3	0*	–
EF4112_4%Si	15.1 ± 0.1	1.2*	47.6 ± 0.3	18.8 ± 0.2	1.0 ± 0.1	–	–	0.2*	0.2*	0.5*	14.2 ± 0.3	0.5*	–
EF6101_6%Si	19.3 ± 0.1	1.8*	45.6 ± 0.3	16.6 ± 0.2	0.9 ± 0.1	–	–	0.1*	0.3*	1.3*	13.6 ± 0.3	0.7*	–
EF4201_4%Si	29.2 ± 0.2	6.3 ± 0.2	31.8 ± 0.2	17.1 ± 0.2	1.2 ± 0.1	–	–	0.2*	0.7*	1.0*	12.2 ± 0.3	0.3*	–
EF6311_6%Si	35.4 ± 0.2	14.6 ± 0.2	16.8 ± 0.1	16.8 ± 0.2	1 ± 0.1	–	–	0.1*	2.2 ± 0.1	1.2*	11.5 ± 0.3	0.4*	–

* Indicates that the scale factor of the related phase was maintained fixed during the refinement.

Table 4
Agreement factors (R_p, R_{wp}, χ^2) between calculated and measured data for each analysed fuel plate (%).

	Agreement factors (%)			
	R_p	R_{wp}	R_{exp}	χ^2
IRISTUM_0%Si	4.8	6.3	2.2	8.6
IRISTUM_2.1%Si	4.8	6.4	2.2	8.2
IRIS1_0%Si	4.8	6.4	2.2	8.8
IRIS3_0.3%Si	6.7	8.1	3.1	4.1
IRIS3_2.1%Si	6.3	7.7	3.8	4.1
IRIS4_0%Si	6.3	7.8	3.6	4.6
IRIS4_2.1%Si	5.7	7.2	3.5	4.2
EF4112_4%Si	6.2	7.3	3.8	3.6
EF6101_6%Si	6.7	8.2	3.7	5.2
EF4201_4%Si	6.2	7.5	3.2	5.6
EF6311_6%Si	5.1	6.3	2.5	6.6

analysis are compared. A general good agreement must be stressed: discrepancies between measured and expected values are lower than 2 wt%. They can very probably be explained by the difficulty to fit accurately the main Al Bragg peak (111), as it overlaps with the most intense Bragg peak (110) of γU–Mo.

The quantification of Si precipitates remaining in the matrix after fuel plate fabrication appears to be inaccurate if only the weight fraction of the Si crystal structure is considered. Indeed this phase could not be identified in the three samples with matrix containing the lowest Si quantity (IRIS3_2.1Si%, IRIS4_2.1Si% and IRISTUM_2.1%Si) while in the four other fuel plates (EF4112_4%Si, EF6101_6%Si, EF4201_4%Si, EF6311_6%Si) the Si concentrations had to be estimated manually since they could not be refined. In other words, for these last four samples, the scale factor of the Si phase has been optimised to match the (111), (220) and (311) most intense Si Bragg lines: many simulations (test/error) were performed for that purpose.

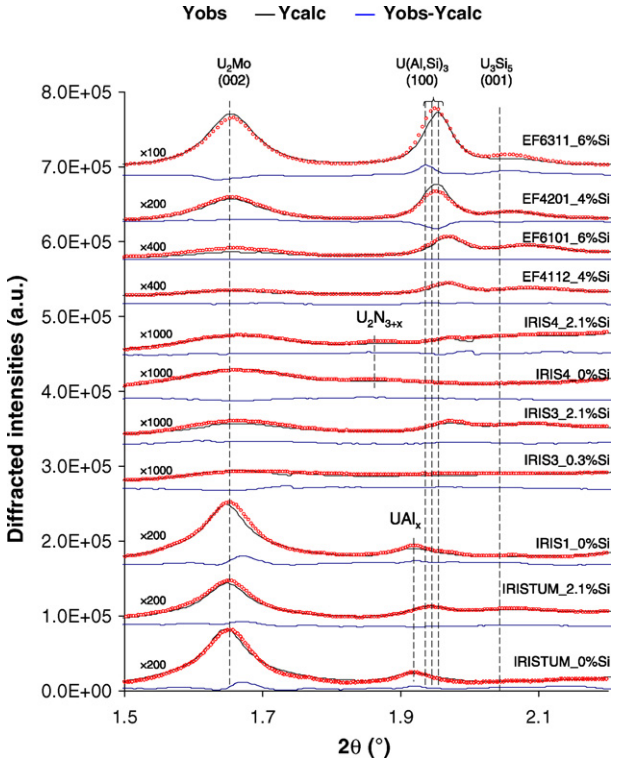

Fig. 3. SiRDL components in the 11 analysed full size plates. Zoom in the [1.5–2.2] 2θ range of the diffraction patterns shown in Fig. 2 with however intensities multiplied by a factor ranging from 100 to 1000 and with *Y*-offset modified.

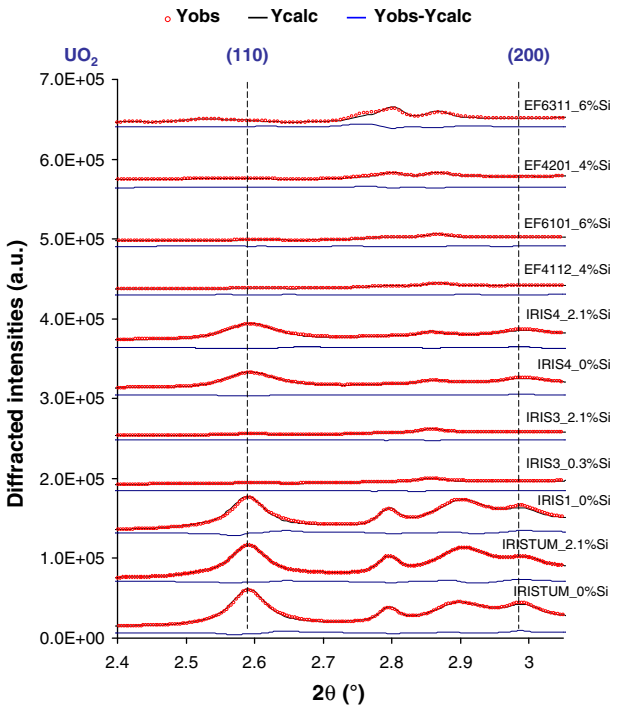

Fig. 4. Illustration of the *oxidation level measured in* 11 fuel plates. Zoom in the [2.4–3.1] 2θ range of the diffraction patterns shown in Fig. 2 with however intensities multiplied by a factor 10 and *Y*-offset modified.

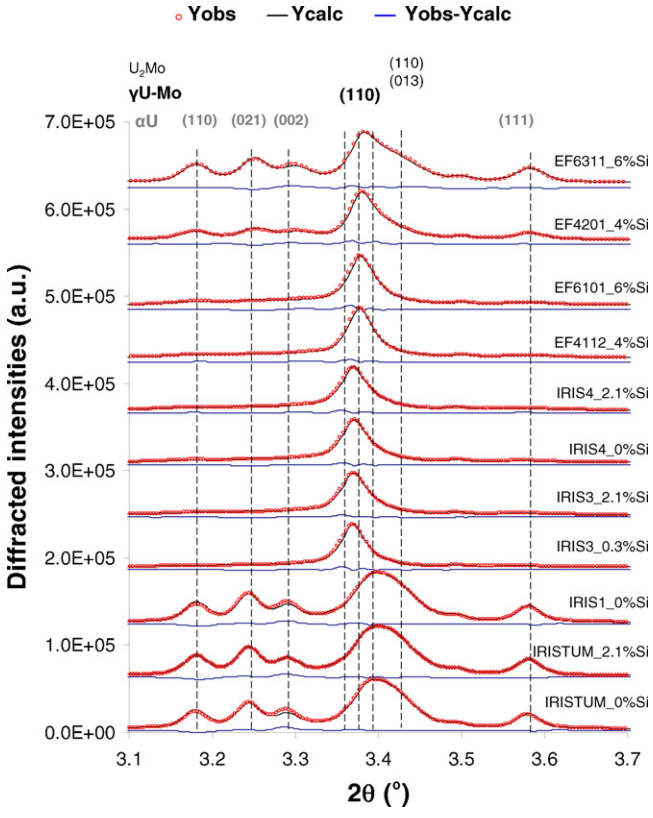

Fig. 5. Illustration of the γU–Mo destabilisation in on 11 fuel plates. Zoom in the [3.1–3.7] 2θ range of the diffraction patterns shown in Fig. 2.

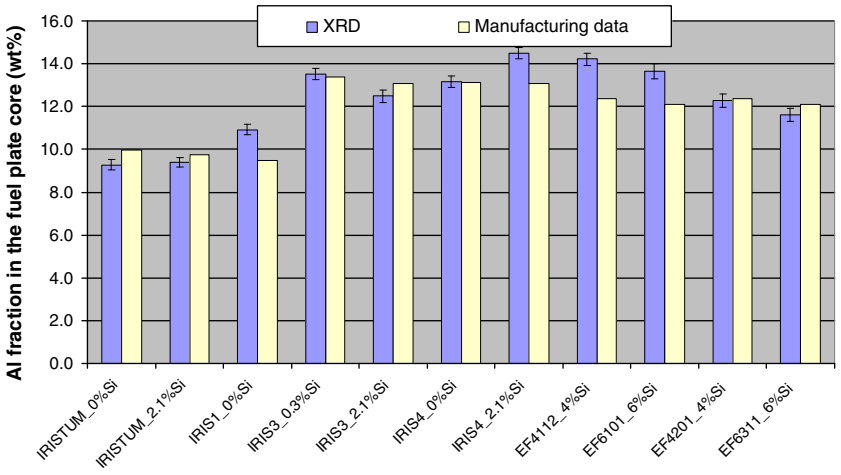

Fig. 6. Comparison between Al weight fractions provided by the manufacturer and those measured by XRD at 87 keV.

The obtained values (given in Table 3) which make however sense relate to Si weight fraction in the meat not in the matrix (see Table 1 for numerical differences). They are close to those derived from the knowledge of both the Si used for each fuel plate fabrication and the measurement of Si inside the SiRDL (cf. § 3.6). Three reasons may explain this relative low sensitivity of high energy X-ray diffraction for measuring Si precipitate weight fractions. First the Si weight fraction in the meat is weak: it never exceeds 0.8 wt% before fuel plate manufacturing and this quantity is even lower in the analysed samples because Si has diffused towards the U–Mo particles to form a SiRDL (i.e. new phases). Second the scattering factor of Si at 87 keV is weak. Third the overlap of some Si Bragg lines (a_0 = 5.43 Å, $Fd\bar{3}m$) with those coming from UO_2 (a_0 = 5.47 Å, $Fd\bar{3}m$) may induce refinement difficulties.

3.3. γU–Mo decomposition rates

Accurate quantification of the decomposition rate has been performed by defining four ratios (αU_ratio, U_2Mo_ratio, γU–Mo-a_ratio and γU–Mo-b_ratio) calculated for each sample from weight fractions given by the Rietveld analysis of XRD patterns. The formula used for their calculations are:

$$\alpha\text{U\_ratio} = \frac{W_{\alpha U}}{(W_{\alpha U} + W_{U_2Mo} + W_{\gamma\text{U-Mo-a}} + W_{\gamma\text{U-Mo-b}})}$$

$$U_2\text{Mo\_ratio} = \frac{W_{U_2Mo}}{(W_{\alpha U} + W_{U_2Mo} + W_{\gamma\text{U-Mo-a}} + W_{\gamma\text{U-Mo-b}})}$$

$$\gamma\text{U-Mo-a\_ratio} = \frac{W_{\gamma\text{UMo-a}}}{(W_{\alpha U} + W_{U_2Mo} + W_{\gamma\text{U-Mo-a}} + W_{\gamma\text{U-Mo-b}})}$$

$$\gamma\text{U-Mo-b\_ratio} = \frac{W_{\gamma\text{UMo-b}}}{(W_{\alpha U} + W_{U_2Mo} + W_{\gamma\text{U-Mo-a}} + W_{\gamma\text{U-Mo-b}})}$$

The values for each studied fuel plate are gathered in Table 5.

Compared to conventional laboratory XRD, these diffraction measurements (using high energy X-ray beams) will not only provide the in-depth characterisation of huge number of particles but also give an accurate measurement of the U_2Mo weight fraction. As already described elsewhere [25], the high signal to noise ratio obtained here allows the accurate measurement of low intensity Bragg peaks ((002) and (101)) which help considerably in evaluating the intensity of the (103), (110) and (004) most intense Bragg lines of the U_2Mo phase, as these lines strongly overlap with the (110) Bragg line of γU–Mo-a and/or γU–Mo-b phase.

The main source of errors in these calculations is related to the presence in some fuel plates of a αU phase exhibiting a monoclinic distortion. It is referred to as α″U in the literature [27] but both its space group and crystal structure have not been yet determined. For the samples containing this α″U phase, its weight fraction (and thus the αU_ratio) has been calculated using the characteristics of αU (space group and crystal structures). Note that the lattice parameters of this phase which are indicated in Table 2 for each fuel plate have also been refined using the space group of αU (CmCm).

3.4. Mo concentration in U–Mo particles and in the different U–Mo phases

Even if the Mo concentration in the U–Mo particles has already been characterised by ICP, the calculation of this parameter using XRD results may be fruitful.

It is well known that for Mo concentrations ranging from 1 to about 16 wt%, Mo is in a solid solution in the γU phase, i.e. the γU–Mo cell parameter is directly linked to the Mo concentration in this phase [28]. Since the cell parameters of the γU–Mo-a and γU–Mo-b phases have been refined for each fuel plate (cf. Table 2), the Mo weight content in these components of the Mo particles can be determined ($X^{Mo}_{\gamma\text{U-Mo-a}}$, $X^{Mo}_{\gamma\text{U-Mo-b}}$).

The Mo concentration in U_2Mo can be readily calculated ($X^{Mo}_{U_2Mo}$ = 16.9 wt%).

The case of the Mo solubility in αU is more difficult to handle but it clearly appears to be lower than in γU–Mo and U_2Mo and can be neglected at this step. To our best knowledge, a unique study deals with the Mo solubility limit in αU [27]. It is supposed to be very low (below 1 at%) and higher concentrations should induce complex structural transitions: β-U is stable for Mo concentrations ranging from 1 and up to 2.2 at%, αU (or α′U) for Mo concentrations between 2.2 and 6.2 at%, α″U (monoclinic crystal structure) for higher Mo concentrations (between 6.2 and 11.4%). This last phase transition (from α′U to α″U) has been attributed to the increase of the γ angle in the structure (up to 92°).

As a conclusion, the Mo weight concentration in U–Mo particles can be derived using the equation:

$$X^{Mo}_{\text{U-Mo-particules}}(\text{XRD}) = X^{Mo}_{U_2Mo} \times (U_2\text{Mo\_ratio}) + X^{Mo}_{\gamma\text{UMo-a}} \times (\gamma\text{U-Mo-a\_ratio}) + X^{Mo}_{\gamma\text{UMo-b}} \times (\gamma\text{U-Mo-b\_ratio})$$

Errors associated with these $X^{Mo}_{\text{UMo-particules}}$(XRD) values have been determined assuming that the cell parameters of the γU–Mo-a

Table 5
Influence of the U–Mo particle microstructure and post-fabrication thermal treatment conditions on the measured αU. U_2Mo, γU–Mo-a and γU–Mo-b weight fractions in U–Mo particle meat (the phases making the protective layers are not taken into account).

	Post manufacturing thermal treatment	U–Mo powder fabrication method	αU_ratio	U_2Mo_ratio	γU–Mo-a_ratio	γU–Mo-b_ratio	γU–Mo_ratio
IRISTUM_0%Si	425 °C—2 h	Ground	39.9 ± 0.5	10.0 ± 0.3	6.8 ± 0.8	43.3 ± 0.6	50.1 ± 0.7
IRISTUM_2.1%Si			39.7 ± 0.5	7.6 ± 0.2	10.8 ± 0.9	41.9 ± 0.6	52.7 ± 0.8
IRIS1_0%Si			39.6 ± 0.5	10.1 ± 0.3	16.8 ± 0.3	33.5 ± 0.5	50.3 ± 0.8
Average			*39.7 ± 0.5*	*9.3 ± 1.4*	*12 ± 5*	*40 ± 5*	*51.0 ± 1.4*
IRIS3_0.3%Si	425 °C—2 h	Atomised	15.9 ± 0.2	1.7*	71.9 ± 0.9	10.5 ± 0.3	82.4 ± 1.3
IRIS3_2.1%Si			20.6 ± 0.4	2.1 ± 0.2	58.7 ± 0.1	18.6 ± 0.5	77.3 ± 1.4
IRIS4_0%Si			21.5 ± 0.3	4.1*	56.5 ± 0.7	16.1 ± 0.3	73.4 ± 1.1
IRIS4_2.1%Si			20.1 ± 0.4	3.1 ± 0.2	57.2 ± 0.9	18.7 ± 0.4	75.1 ± 1.3
EF4112_4%Si			18.9 ± 0.3	1.4*	56.3 ± 0.7	22.3 ± 0.4	78.6 ± 1.1
EF6101_6%Si			22.9 ± 0.3	2.1*	54.1 ± 0.8	19.7 ± 0.4	73.9 ± 1.2
Average			*20 ± 3*	*2.4 ± 1.0*	*59 ± 6*	*18 ± 4*	*77 ± 3*
EF4201_4%Si	475 °C—2 h	Atomised	34.1 ± 0.5	7.3 ± 0.2	37.1 ± 0.5	20 ± 0.4	57.1 ± 1.5
EF6311_6%Si	475 °C—4 h	Atomised	41.8 ± 0.5	17.3 ± 0.3	19.9 ± 0.3	19.8 ± 0.4	39.7 ± 1.2

* Indicates that the scale factor of the related phase was maintained fixed during the refinement.

and γU–Mo-b phases have been refined within ±0.001 Å. This error is very probably overestimated.

The Mo concentrations in U–Mo particles obtained with this methodology for each full size plate are gathered in Table 2 and compared to the values measured by ICP ($X^{Mo}_{UMo\text{-}particules}$ (ICP)) in Fig. 8. A good general agreement can be found.

However for 8 fuel plates, $X^{Mo}_{UMo\text{-}particules}$ values are lower than those measured by ICP. This underestimation suggests that the Mo concentration in the αU (and in the associated distorted phases) phase is not zero in these cases. This has been calculated:

$$X^{Mo}_{\alpha U} = 100 \times \left(\frac{X^{Mo}_{UMo\text{-}particules}(ICP) - X^{Mo}_{U\text{-}Mo\text{-}particules}(XRD)}{\alpha U\_ratio} \right)$$

Results for each full size plate are reported in Table 2.

As expected Table 2 shows that the presence of Mo in the αU phase is systematically associated with a distortion of the lattice, i.e. a lower *c* parameter (see Section 3.3). In these cases, αU is thus very probably the α″U phase.

3.5. Protective layer (SiRDL and oxide) thickness determination for atomised U–Mo particles

The main goal of this section is to measure the thickness of the SiRDL obtained around U–Mo atomised particles after fuel plate manufacturing, with significant Si concentration (>2 wt%) in the AlSi matrix.

However this appears to be a very difficult task for at least three reasons.

First this SiRDL has a very irregular shape around a given U–Mo particle.

Second the SiRDL thickness may strongly fluctuate from an U–Mo particle to another inside the same fuel plate. As a consequence their appropriate measurements would require a SEM mapping with very high resolution of large areas in the fuel plate meat as well as the development of enhanced image analysis codes which are not yet available.

Third during sample preparation U–Mo particles are not always cut along an equatorial plane: the results provided by 2D imaging techniques (scanning electron microscopy (SEM)) could lead to a systematic overestimation of the real SiRDL thicknesses.

Based on the quantitative XRD measurement detailed in a previous section (cf. 3.1), an average value for the protective shell of the U–Mo particles in the meat can be derived by assuming a spherical shape for the U–Mo particles, and a full density for the phases making the layer (10.5, 8.9 and 6.8 g cm^{-3} are considered as theoretical densities for polycrystalline UO_2, U_3Si_5 and $U(Al,Si)_3$) [29]. Note that this calculation is only valid for atomised powders and not for ground powders because of their very irregular shapes. A precise knowledge of the UMo powder granulometry is also required.

It has been chosen to apply this method not only to the measurement of SiRDLs but also to oxide layers whose thickness seems to be more homogeneous are U–Mo particles. This difference between the characteristics of both layers is illustrated by Fig. 7. It shows two OM and SEM images of U–Mo particles either surrounded by a UO_2 or a Si rich protective layer.

Therefore, the average thickness given by microscopy and XRD measurements should be in better agreement for oxide layers than for Si-rich ones.

The relationship between the thickness of a given protective layer and the diameter of the U–Mo core of the particles (D) has been found to be $e = 0.0004 \times D^2 + 0.0902 \times D + 0.0013$ and $e = 0.0008 \times D^2 + 0.0892 \times D + 0.0027$ for the pre-oxidised and standard U–Mo powders, respectively. The detailed demonstration of these equations is the subject of a forthcoming paper.

The thicknesses of the oxide and Si-rich shells have been calculated for each sample of interest. The results are indicated in Table 6 and compared to the values obtained by SEM. As expected values derived from XRD measurements are systematically lower than those measured by SEM. If a large discrepancy can be seen in the SiRDL thicknesses obtained by both techniques, a better agreement is noted for oxide shells. Larger uncertainties in the results obtained by microscopy for oxide layers must however be mentioned.

3.6. Location of Si in the as-fabricated samples

When Si has been added to the matrix, this element can either be found in precipitates in the Al matrix or in the SiRDL after fuel plate manufacturing. However the applied technique (diffraction with high energy X-ray beams) turns out to be poorly sensitive to the Si crystal structure (see Sections 3.1 and 3.2). The fraction of Si located in the matrix as precipitates can however be estimated. It is based on the accurate quantification of the Si weight fraction in the SiRDL and the precise knowledge of the Si quantities added to the matrix during the fuel plate manufacturing step.

Therefore the SiRDL weight fraction in the meat (W_{SiRDL}) can be readily defined by:

$W_{SiRDL} = \sum_j W_j$ where W_j is the weight fraction of each phase making the SiRDL.

Only two possible components for this protective shell have been identified by XRD: U_3Si_5 and $U(Al,Si)_3$. As proposed by Dwight, Silicon may insert in the UAl_3 crystal structure and occupy Al sites. It can thus be considered as a solid solution: the Si content in this

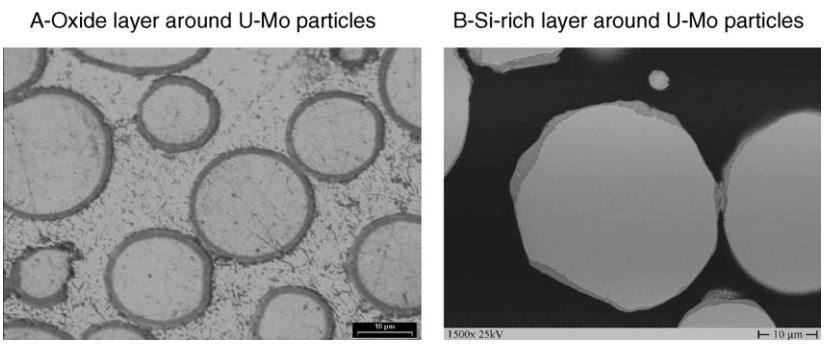

Fig. 7. Comparison of the shape of the oxide (optical micrograph (A)) and Si-rich layers (SEM picture (B) [17]) around U–Mo particles. They are homogeneously thick around U–Mo particles in the case of oxide and very heterogeneous in the case of Si-rich layers.

Table 6
Comparison between the average thicknesses of oxide and Si-rich protective layers in the 8 fuel plates containing U–Mo atomised powder as determined from high energy XRD and microscopy [31].

	Post manufacturing thermal treatment	Average thickness of the protective layers around U–Mo particles (μm)			
		XRD		Microscopy	
		Oxide	Si-rich	Oxide	Si-rich
IRIS3_0.3%Si	425 °C–2 h	0.06	–	–	–
IRIS3_2.1%Si		0.13	0.11		
IRIS4_0%Si		1.11	–	1.0–1.5	–
IRIS4_2.1%Si		1.15	0.09		
EF4112_4%Si		0.03	0.16	–	0.7
EF6101_6%Si		0.06	0.36	–	0.6
EF4201_4%Si	475 °C–2 h	0.03	0.40	–	0.8
EF6311_6%Si	475 °C–4 h	0.03	0.84	–	1.3

phase can be determined provided that the $U(Al,Si)_3$ lattice constant is known [30]. The Si weight fraction in this phase can thus be derived using this method. Depending on its Si content, it ranges from 0.08 to 0.12 wt% in $U(Al,Si)_3$ for the studied samples.

Therefore the weight fraction of Si in the SiRDL can be calculated from the analysis of XRD patterns:

$W^{Si}_{SiRDL} = \sum_j Y_j \times W_j$, Y_j being the Si weight fraction in each j phase making the SiRDL (it equals 0.17 in U_3Si_5). For the fuel plates with a Si-doped matrix, Table 7 shows this Si fraction in the SiRDL (however converted in atomic percents). A good agreement can be noticed between these values and those measured by EDX (Energy dispersive Spectrometry) or EPMA (Electron Probe micro Analysis) [17,31–33].

It means that using the known initial quantity of Si added to the matrix ($W^{Si}_{Al/initial\text{-}state}$), the weight fraction of Si still located in the precipitates in the as manufactured fuel plates is:

$$W^{Si}_{precipitates} = W^{Si}_{Al/initial\text{-}state} - W^{Si}_{SiRDL} = W^{Si}_{Al/initial\text{-}state} - \sum_j Y_j \times W_j$$

The error associated with the normalised ratios of Si in Si precipitates or of Si in the SiRDL ($W^{Si}_{SiRDL}/W^{Si}_{Al/initial\text{-}state}$ and $W^{Si}_{precipitates}/W^{Si}_{Al/initial\text{-}state}$, respectively) is estimated to a few percents. Note that contrary to the SiRDL thickness determination this calculation does not depend on the density of its components.

The Si fraction in the SiRDL and the Si precipitates are given in Table 8 for each relevant fuel plate.

4. Study of the γU–Mo decomposition

This section has three goals: (i) defining the main mechanism for U–Mo phase decomposition under each fabrication conditions, (ii) quantifying the rate of decomposition of the γU–Mo phase and (iii) evaluating the influence of the U–Mo particle microstructure on the two first subjects of interest.

This discussion is based on the results gathered in Table 2 and Table 5 which demonstrate the influence of both manufacturing conditions and U–Mo particle microstructure on the rate of γU–Mo decomposition and on the characteristics of the

Table 7
SiRDL elementary and crystallographic compositions as measured by XRD and by EDX/EPMA [17,31–33]. The characteristics of the $U(Al,Si)_3$ phase are also provided for each fuel plate [30].

	U–Mo micro-structure	Post manufacturing thermal treatment	SiRDL composition as determined by XRD (wt%)		$U(Al,Si)_3$ characteristics		Si atomic composition in the SiRDL (at%)		
			$U(Al, Si)_3$	U_3Si_5	A_0 (Å)	Si/(Al + Si) (%at)	XRD	EDX	EPMA
IRISTUM_2.1%Si	Ground	425 °C–2 h	12	88	4.21	23	56	20–55	
IRIS3_2.1%Si	Atomised	425 °C–2 h	14	86	4.16	44	54	50	
IRIS4_2.1%Si			8	92	4.16	44	59	53	
EF4112_4%Si			24	76	4.16	44	53	50	
EF6101_6%Si			20	80	4.16	44	55		38
EF4201_4%Si	Atomised	475 °C–2 h	41	59	4.19	32	43		33
EF6311_6%Si	Atomised	475 °C–4 h	64	36	4.19	32	34	36	

Table 8
Influence of the AlSi matrix and U–Mo microstructures on the Si repartition (in the SiRDL or in the matrix) in as-fabricated fuel plates.

	Post manufacturing thermal treatment	U–Mo micro-structure	AlSi powder	Location of the Si elements in the as-fabricated fuel plates (wt%)		Si in the SiRDL (weight fraction (%) of the matrix)
				SiRDL	Si precipitates in the matrix	
IRISTUM_2.1%Si	425 °C—2 h	Ground	Alloy	100*	0*	2.1
IRIS3_2.1%Si	425 °C—2 h	Atomised	Alloy	30.6	69.4	0.6
IRIS4_2.1%Si				19.5	80.5	0.4
EF4112_4%Si	425 °C—2 h	Atomised	Mixing	19.0	81.0	0.8
EF6101_6%Si				30.6	69.4	1.8
EF4201_4%Si	475 °C—2 h	Atomised	Mixing	46.7	53.3	1.9
EF6311_6%Si	475 °C—4 h	Atomised	Mixing	54.9	45.1	3.3

* Note that calculations give 103% of Si located in the SiRDL. Results were thus slightly corrected.

destabilisation products (Mo content and lattice parameters), respectively. A qualitative comparison of the destabilisation rate of the γU–Mo phase in these samples is also provided by Fig. 5 where the 11 collected patterns in the [3.1;3.7] 2θ range are shown.

4.1. Atomised powders in full size plates that underwent a post-manufacturing thermal treatment at 425 °C

Six samples have been considered for this analysis (IRIS3_0.3%Si, IRIS3_2.1%Si, IRIS4_0%Si, IRIS4_2.1%Si, EF4112_4%Si, EF6101_6%Si). As shown in Table 2, the main products of this decomposition are a γU–Mo phase enriched in Mo (with about 10.4 wt%) and the α″U phase also containing 2.2 wt% (i.e. 5 at%) of Mo (see Sections 3.3, 3.4). The γ angle in the α″U crystal structure has been evaluated to 90.6° by Lebail fitting of the profile of this phase (the Cm space group for α″U has been used). When using an orthorhombic structure (with CmCm space group), the α″U lattice parameters have been found to be: a = 2.872 Å, b = 5.848 Å, c = 4.935 Å.

To illustrate the absence of αU or α′U crystal structures in the as-fabricated full size plates with atomised U–Mo particles, Fig. 9A shows the agreement between measured and calculated intensities of (131) αU Bragg line in the EF4112_4%Si fuel plate. Both structural model and the space group (Cmcm) of this phase do not match perfectly.

A quantitative comparison of the results of the Rietveld analysis in this set of samples shows that the decomposition rates of the γU–Mo phase are quite close. The αU_ratio evolves between 15.9 and 22.1%, γU–Mo_ratio between 73.4 and 82.4% (cf. Table 5). Moreover even if the U_2Mo phase has been unambiguously identified (cf. Fig. 3), its amount does never exceed 3.1%.

However it seems that the IRIS3_0.3%Si exhibits an unusually low destabilisation ratio. Further investigations together with the manufacturer will be undertaken to elucidate this problem: a complementary XRD analysis of the fresh IRIS2_0%Si fuel plate which has been produced in the same conditions than IRIS3_0.3%Si and which has the same composition has to be performed.

4.2. Ground powders in full size plates that underwent a post-manufacturing thermal treatment at 425 °C

Three fuel plates (IRIS1_0%Si, IRISTUM_0%Si, IRISTUM_2.1%Si) have been manufactured with U–Mo ground powder and subsequently thermally annealed at 425 °C.

XRD analyses have shown that the main components in the ground U–Mo particles are as expected γU–Mo enriched in Mo (with about 14.8 wt%) [34] and the α′U phase (a = 2.859 Å, b = 5.843 Å, c = 4.964 Å) [35] (see Table 5 and Table 2). Furthermore U_2Mo can not be considered anymore as a trace phase. Its ratio in U–Mo particles increased up to 10.1 wt%, i.e. almost 5 times the ratio measured in fuel plates manufactured in the same conditions but with atomised powders.

Based on the hypothesis that Mo is only present in γU–Mo phases and in U_2Mo, an approximate Mo weight fraction in the U–Mo particles has been calculated (see Section 3.4). They are in good agreement with values given by ICP measurements confirming that the Mo content of the α′U phase in these ground particles is very low if not zero (see Fig. 8).

This conclusion disagrees with a previous XRD study performed with laboratory equipments on samples taken from the same IRISTUM plates [35]. However, due to a lack of signal to noise ratio in their measurement, these authors could not identify the U_2Mo phase and the Mo quantity present in this phase could not be taken it into account in their calculations.

By comparing the composition of the U–Mo particles in the three fuel plates considered in that section, a relatively good agreement can be found especially in the case of the IRIS1_0%Si and IRISTUM_0%Si plates.

Finally one can conclude: (i) the results discussed in that section are robust and (ii) that the industrial process applied for manufacturing fuel plates with ground powders leads to reproducible results.

4.3. Atomised powders in full size plates that underwent a post-manufacturing thermal treatment at 475 °C

Annealing nuclear fuel plates at 475 °C clearly favours the destabilisation of the γU–Mo phase (see Table 2 and Table 5). At this temperature the first step of the destabilisation (after 2 h, i.e. for the EF4201_4%Si fuel plate) leads to mainly the growth of α″U and a Mo enriched γU–Mo phase (13 wt%), the formation of U_2Mo being however significantly larger to what was observed at 425 °C. At a second step (after 4 h, i.e. for the EF6311_6%Si fuel plate), the amount of γU–Mo-b does not evolve much, and the destabilisation seems to mainly lead to the growth of U_2Mo and α′U at the expense of γU–Mo-a and α″U. Concerning the Mo content of the α′U phase, it seems to be low but not zero in the EF 4201_4%Si fuel plate, when increasing the post-treatment duration leads to a depletion of the α′U phase in Mo and an increase of the c parameter of this phase: its lattice constants become very close to those observed on fuel plates made with ground powders (see Table 2). Fig. 9B, illustrating for the EF6311_6%Si fuel plate the good agreement between measured and calculated data for the (131) αU Bragg line, confirms that the crystal structure and space group used for αU are appropriated in this case.

4.4. Influence of U–Mo particles oxidation or Si addition to the matrix

In this section, the influence of a protective shell on the destabilisation of the γU–Mo phase in atomised particles has been investigated. Two kinds of protective shell are considered: a Si rich (SiRDL) one and an oxide one. By comparing first the αU, U_2Mo

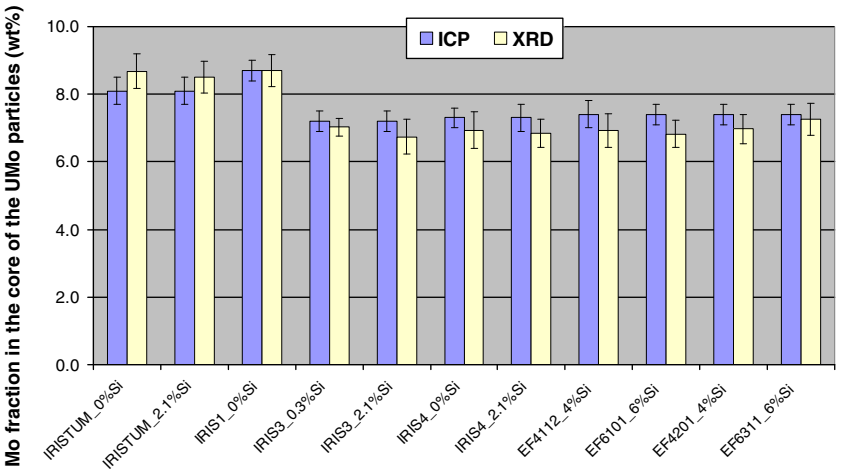

Fig. 8. Comparison between the Mo weight fractions in the U–Mo particles (meat only) as obtained by ICP and XRD.

and γU–Mo_ratios in two samples containing different Si concentrations in the matrix it can be shown that the limited fluctuations of this parameter do not induce any significant modification of the γU–Mo stability. The case of IRIS3 fuel plates will not be considered here since the composition of the IRIS3_0.3%Si seems to be problematic. Instead the behaviour of IRIS4 fuel plates will be discussed.

Indeed these two fuel plates which have been produced in exactly the same conditions (temperature treatment and hot rolling machine settings), exhibit the same αU, U_2Mo and γU–Mo_ratios if standard deviations are taken into account (cf. Table 5). However in the XRD measurements performed in that work, the whole U–Mo particles are probed. Therefore, this analysis is only sensitive to volume destabilisations: it is likely that a destabilisation only of the interface between the protective shell and the U–Mo meat (i.e. occurring in a thin outer part of the meat) would not have been detected by this technique. Complementary measurements are needed to tackle definitely this issue.

5. Oxide layer

5.1. Crystallographic composition

If UO_2 is clearly the main crystallographic component of these layers, this is not the only one. Indeed at least two additional phases have been identified in the plates with high oxidation rates: UN in the plates made with ground powders (IRIS1_0%Si, IRISTUM_0%Si, IRISTUM_2.1%Si) and U_2N_{3+x} (space group $Ia\bar{3}$, $a_0 = 10.65$ Å) mainly in the plates made with atomised UMo powders (IRIS4_0%Si, IRIS4_2.1%Si) [36].

Fig. 10, which shows two zooms in the XRD pattern measured on IRIS4_0%Si, illustrates the presence of this last phase. Note that SEM/EDX measurements performed on IRIS4_0%Si and IRIS4_2.1%Si fuel plates confirm the heterogeneity of this UO_2 protective layer and underline the presence of U_xN_y phases.

It must be mentioned that the refined profile for the UO_2 Bragg lines is not fully satisfactory using an undistorted UO_2 crystal structure suggesting that a distortion exists (cf. Fig. 10B). Either a gradient in the O content of this oxide layer with the presence of UO_{2+x} phase or strains due to the U–Mo substrate could explain this observation. However to quantify the uranium oxide weight fraction in these fuel plates, the undistorted UO_2 crystal structure has only been taken into account. Diffraction experiments using nano X-ray beams would probably enable a better description of the composition of these nitride and oxide layers [37]. These experiments should be performed on U–Mo particles taken from the powder (i.e. before fuel plate manufacturing) to check for the presence of U_xN_y phases. It would allow a better understanding of the unexpected presence of these phases. This discussion is however out of the scope of the present paper.

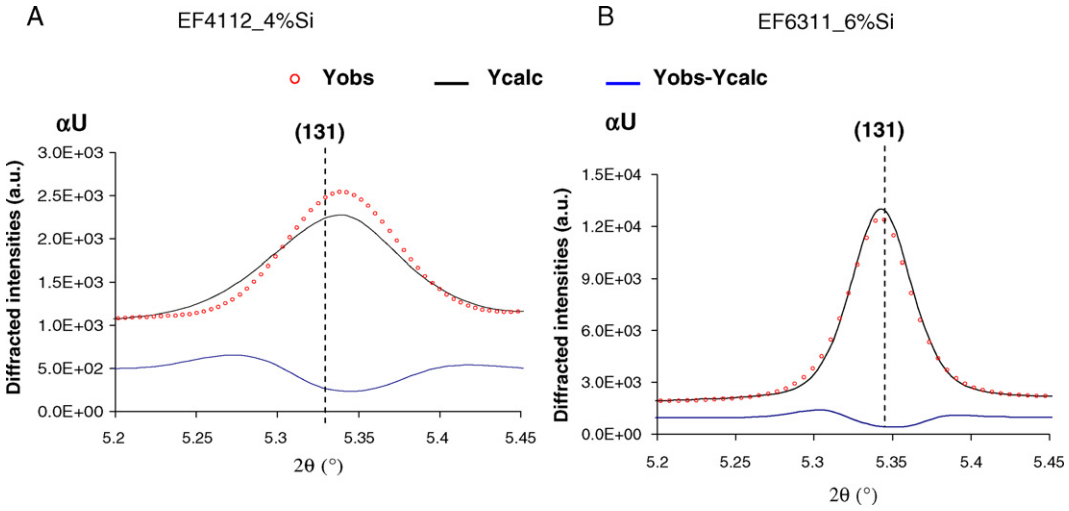

Fig. 9. Lower quality of the fit for the αU phase in the diagrams collected on samples manufactured at 425 °C (during 2 h) than for a fuel plate produced at 475 °C (during 4 h).

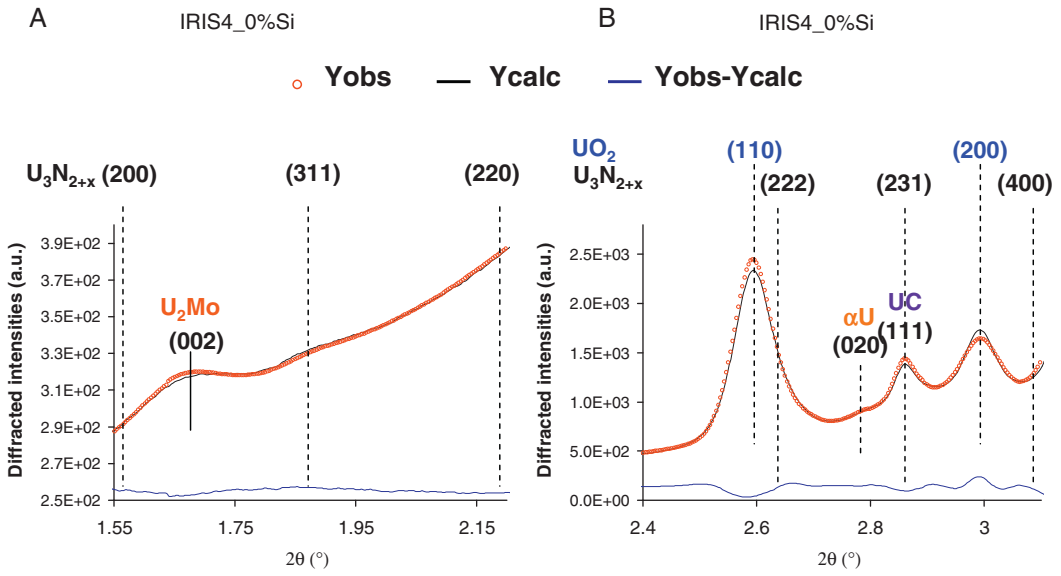

Fig. 10. Comparison between measured and calculated XRD diagrams on the IRIS4_0%Si fuel plate in two limited 2θ ranges ([1.55; 2.2°] (A) and [2.4; 3.1°] (B)). Evidence for the distortion of the UO_2 crystal structure and for the presence of U_2N_{3+x} in the oxide protection layer around U–Mo particles.

5.2. Oxide layer weight fractions in full size plates

Fig. 4 shows the measured intensities of the (110) and (200) most intense Bragg lines of UO_2 in the 11 characterised fuel plates. It provides a first indication of their UO_2 content.

Concerning the fuel plates made with atomised powders (IRIS4_0%Si and IRIS4_2.1%Si), the UO_2 weight fraction was expected to be identical since the pre-oxidised U–Mo powders were coming from the same batch (production and oxidation) and that the nuclear fuel plate hot-rolling process was also identical,. As shown in Table 3, this is the case when standard deviations of the fitting procedure are taken into account. A larger discrepancy is observed on the U_xN_y content of these layers. It is larger than 20% for IRIS4_0%Si and less than 15% for IRIS4_2.1%Si.

Oxide fractions in ground and atomised U–Mo particles can be compared. In the case of ground powders, the oxidation is systematic during manufacturing affecting not only the outer surface of the particle but also the inner part: after rolling some oxide stringers can be observed [15]. The oxide fraction is very close in IRIS1_0%Si and IRISTUM_0%Si and definitely lower in IRISTUM_2.1%Si (see Table 3). However these three fuel plates exhibit a lower UO_2 weight fraction than the IRIS4 fuel plates. Taking into account the larger specific surface of ground powders and the presence of oxide stringers, it can be concluded that the average thickness of the oxide layer is significantly larger in IRIS4 fuel plates than in those made with ground powders.

5.3. Oxide layer thickness

The average thickness of the oxide protective layer around U–Mo particles in both fuel plates IRIS4_0%Si and IRIS4_2.1%Si has been obtained thanks to the equation mentioned in section 3.5 and the results of this calculation are given in Table 6. The obtained value (about 1.2 μm) is of the same order than those given by microscopic observations (i.e. between 1.0 and 1.5 μm [31]) which however suffer from large uncertainties.

In each fuel plates made with U–Mo atomised powder UO_2 impurities have also been found. An average thickness of this layer has thus been calculated. For the 8 considered fuel plates, they all are well below 0.08 μm, except IRIS3_2.1%Si for which an average UO_2 shell of 0.13 μm has been measured.

6. Si behaviour during full size plate manufacturing

This section is based on the analysis of 3 tables. Table 6 shows the influence of manufacturing conditions on the SiRDL thickness around atomised U–Mo particles. Table 7 characterises the influence of manufacturing conditions and U–Mo particle microstructures on the SiRDL elementary and crystallographic compositions. Finally Table 8 gives the Si repartition in the meat as a function of both particle and matrix microstructure on the one hand and manufacturing conditions on the other hand.

6.1. Influence of a post-manufacturing thermal treatment at 425 °C

6.1.1. Fuel plates containing atomised U–Mo powders

At this temperature, the composition of 4 fuel plates can be directly compared: IRIS3_2.1%Si, IRIS4_2.1%Si, EF4112_4%Si and EF6101_6%Si. Note that the IRIS3_0.3%Si fuel plate has been disregarded since no trace of SiRDL has been found neither by microscopy nor by diffraction.

First it can be shown that whatever the Si content in the matrix (between 2.1 and 6 wt%), the composition of the SiRDL does not change significantly. Two components have been identified: U(Al, Si)$_3$ and U_3Si_5. In each case, the cell parameter of the U(Al, Si)$_3$ has been found to be 4.16 Å. As a consequence the atomic ratio Si/(Al + Si) in this phase can be evaluated to 44.2 at% (cf. Table 7). Using this XRD characterisation of the SiRDL in the different fuel plates, its elementary composition can be estimated and compared to that found by EDX/EPMA (cf. Table 7). It comes first that whatever the Si content in the matrix, the Si content in the SiRDL in the as-manufactured fuel plates is almost constant (about 50 at%) and very close to what has been measured. Secondly this good agreement can be considered as an additional argument for validating this quantitative analysis using XRD.

Based on the results from XRD and microscopy, it appears that by increasing the Si content in the Al matrix, the SiRDL becomes thicker. From 0.11 μm with 2.1 wt% Si (IRIS3_2.1%Si), it increases up to 0.36 μm when adding 6 wt% Si (EF6101_6%Si).

Finally, the key point of this study seems to be provided by Table 8. It appears that the Si fraction in the SiRDL is higher in IRIS3_2.1%Si (30.6%) than in EF4112_4%Si (19.0%) and in IRIS4_2.1%Si

(19.5%) and almost equivalent to EF6101_6%Si (30.6% or 1.8 wt% of the matrix). Beside the importance of the Si quantity used for manufacturing a fuel plate at a given temperature, it seems that the matrix microstructure has also an importance. Indeed in IRIS3_2.1%Si, the AlSi matrix was an alloyed powder when in EF4112_4%Si and EF6101_6%Si, the AlSi matrix was produced from mixed powders.

6.1.2. Fuel plates containing ground U–Mo powders

The analysis of IRISTUM_2.1%Si composition shows that the SiRDL consists also of $U(Al, Si)_3$ and U_3Si_5 as in the previous case of nuclear fuel plates made of atomised powders (see Table 7 and Fig. 3). However two main differences can be found. Firstly the $U(Al, Si)_3$ phase is Si depleted: its cell parameter (refined to 4.21 Å instead of 4.16 Å for atomised powders) shows that this phase contains twice less Si (the Si/(Al + Si) ratio is 23 at% instead of 44 at%) (cf. Table 7). Secondly the U_3Si_5 amount exceeds from far the values obtained for atomised powders (1.2 wt% in the meat).

Once more the most striking feature of this analysis is given in Table 8: using the U_3Si_5 and $U(Al,Si)_3$ weight concentrations discussed previously and the methodology discussed in section 3.6, it can be demonstrated that no Si precipitates are left in the matrix after the manufacturing step. SEM/EDX investigations corroborate this macroscopic result [32,33]: in addition to thin SiRDL partially protecting ground U–Mo particles, many small particles made of four elements (mainly U and Si but also Al and Mo) have been found in the as-fabricated fuel plate matrix, along with very few Si precipitates. They are definitely less numerous than in for example IRIS3_2.1%Si. The growth of these small U, Si, Al, Mo particles can very probably be explained by the presence in the ground U–Mo powder of a non negligible fraction of very small particles: they have interacted preferentially with Si during fuel plate manufacturing [32].

From a methodological point of view, the analysis of IRISTUM_2.1%Si fuel plate validates the robustness of both the XRD characterisation and the developed methodology for investigating the Si precipitate fraction remaining in the matrix after manufacturing.

6.1.3. Influence of a post-manufacturing thermal treatment at 475 °C

The crystallographic composition of the SiRDL formed after fuel plate manufacturing at 475 °C, is basically identical to the one obtained at 425 °C. Two phases are identified whatever the post-manufacturing thermal treatment duration: U_3Si_5 and $U(Al,Si)_3$ with however a higher cell parameter (4.19 Å) thus indicating a lower Si content [30]. The Si/(Al + Si) atomic ratio in $U(Al,Si)_3$ appears to be about 32% (cf. Table 7). From these crystallographic results, the Si content in the SiRDL has been evaluated (see section 3.6). It comes that the longer the annealing duration, the higher is the $U(Al,Si)_3$ weight ratio in the SiRDL; therefore, the Si content decreases even if the amount of Si added in the matrix was higher (cf. Table 7). Note that the thickness of the SiRDL has been found to reach almost 0.9 μm in the fuel plate containing the highest Si concentration and annealed during the longer duration.

6.2. Possible complementary measurements

The comparison between the thicknesses of the SiRDL as determined by 2D techniques (scanning electron microscopy) and those obtained from volume techniques (high energy XRD) shows a clear difference, the first being systematically lower than the seconds. However if this difference results very probably from the correction of geometrical artefacts created by the use of a 2D characterisation, it should be investigated whether the density of this SiRDL is 100% or lower.

Concerning the crystallographic composition of the SiRDL, it has been shown that at both tested temperatures, it only consists of $U(Al,Si)_3$ and U_3Si_5. Complementary characterisations using a more local probe would be needed mainly to investigate the presence of ternary compounds like UMo_2Al_{20} and $U_6Mo_4Al_{43}$ [37] as found in U–Mo/Al(Si) diffusion couples [38]. This would have three advantages. First a better estimation of SiRDL thicknesses would be obtained. Second a definitive conclusion on the presence of phases with poor in-pile performances (like $U_6Mo_4Al_{43}$ or UAl_4) could be proposed [39]. Finally from a methodological point of view, such a work would be interesting for defining the limits of these macroscopic and volume measurements in describing the slight evolutions of SiRDL composition with manufacturing conditions.

6.3. Optimisation of the manufacturing process

To improve the in-pile behaviour of dispersed U–Mo/Al(Si) fuels, this Si fraction located close to U–Mo particles (for example in the SiRDL) should be optimised. However in this study it has been shown that even in the most favourable tested annealing conditions (475 °C during 4 h) in terms of diffusion, the fraction of Si in the SiRDL never exceeds 60%, i.e. 4 wt% of the matrix (cf. Table 8).

This work has shown three ways for increasing this fraction using this concept (addition of Si to the matrix). However it must be mentioned that recently two techniques have been developed for coating atomised UMo powders with Si: they are based on either physical vapour deposition [40] or solid/solid reactions (annealing at 900 °C under vacuum) [41].

First higher Si quantities have to be added to the matrix (compare fuel plates EF4112_4%Si, EF6101_6%Si). This argument is also supported by the first results of non-destructive examinations performed on E-FUTURE plates after in-pile irradiation [42]: the plates with the highest Si fraction in the matrix exhibit the lowest swelling. However these Si amounts have to remain limited, otherwise some difficulties in this fuel back-end could occur [17]. Second alloyed AlSi powders have to be chosen as a matrix. Even if this result is only based on the comparison of very few samples, it seems that this feature deeply influences the Si diffusion towards U–Mo during the manufacturing and the subsequent thermal treatments. Finally annealing during a larger duration at 425 °C nuclear fuel that contain 6 wt% Si in the matrix seems to be a very promising solution. Indeed the destabilisation of the U–Mo particles has been found to be very low (below 25 wt%), the fraction of Si in the SiRDL is optimal (higher than 50 at%) and the ratio of Si located in the SiRDL pretty elevated (about 30%). As a comparison, manufacturing processes based on annealing at 475 °C seems to be less appropriated whatever the Si content and the duration of the thermal treatment.

7. Conclusion

X-ray diffraction using high energy X-ray beams has been shown to be a very powerful technique to characterise as-fabricated U–Mo/Al(Si) nuclear fuel plates. Indeed based on this measurement, the destabilisation level of U–Mo particles and both the thickness and the compositions (crystallographic and elementary) of the SiRDL have been determined at a macroscopic scale. Moreover access to the repartition of the Si between SiRDL and precipitates in the matrix has been obtained.

The conclusions of this paper are based on the analysis of eleven full size fuel plates.

Both the products and the levels of the γU–Mo destabilisation depend on the manufacturing conditions of the fuel plates but also on the U–Mo particle microstructure. If the obtained results are in agreement with the TTT curve describing the γU8-Mo destabilisation [12], it has been shown that at low destabilisation levels (after

a post-manufacturing thermal treatment at 425 °C during 2 h), the α″U crystal structure in addition to a Mo enriched γU–Mo phase was formed in fuel plates produced with U–Mo atomised particles. It would be interesting to know whether the presence of this phase is systematic at the first stages of the γU-8Mo destabilisation or is related to the initial U–Mo microstructure (and is only found in destabilised atomised particles). The study of fuel plates manufactured in more demanding conditions (with a post-manufacturing thermal treatment at 475 °C during 4 h) with atomised U–Mo particles, shows that this α″U crystal structure has vanished (replaced by α′U) when the weight fraction of U_2Mo has strongly increased at the expense of the Mo enriched γU–Mo phase.

Analyses of fuel plates made of U–Mo ground powders after a post-manufacturing thermal treatment at 425 °C during 2 h have shown a composition very close to that discussed for fuel plates made of atomised particles but annealed at 475 °C during 2 h. The main difference was the lower U_2Mo concentration.

The interest of limiting the post-manufacturing temperature of full size U–Mo/Al(Si) plates at relatively low temperature (425 °C) has been demonstrated. Indeed at higher temperatures (475 °C) a risk of Si depletion of the SiRDL exists. Moreover it seems that the use of alloyed AlSi powder rather than mixed powder significantly improves the Si diffusion towards U–Mo particle during the manufacturing process.

New investigations will be performed in three directions.

From a methodological point of view, it is obvious that this study at a macroscopic scale has to be completed by an analysis of the SiRDL composition at the U–Mo particle scale [37]. It would be very useful to evaluate its heterogeneity, measure its density, and attest the presence of trace phases.

Second the determination of the α″U space group and precise crystal structure would be of first interest. Moreover the influence of second order parameters in the U–Mo/Al(Si) nuclear fuel manufacturing process as the kind of cladding or the presence of Si precipitates should be also quantified. For this last prospect, the set of samples described here was too restricted and would not have provided definitive conclusions.

Finally screening tests to optimise the thermal treatment duration at 425 °C (and thus SiRDL characteristics) should be performed. This study could be carried out using smaller samples (miniplates) that are less expensive than full-size plates [43,44].

Acknowledgements

The authors are grateful to X. ILTIS (CEA, DEC) for providing the U–Mo powder granulometry measurements and the microscopic and elementary characterisations of the SiRDL in these nuclear fuel plates. F. CHAROLLAIS, S. MAILLARD (CEA), B. STEPNIK (AREVA-CERCA), R. JUNGWIRTH and W. PETRY (TUM) are also acknowledged for their advices and careful reading of this paper. Finally C. TANGUY is warmly thanked for her experimental and technical contribution to this work.

References

[1] W.T. Eeles, A.L. Sutton, Acta Cryst. 16 (1963) 575.
[2] A.C. Lawson, C.E. Olsen, J.W. Richardson Jr., M.H. Mueller, G.H. Lander, Acta Cryst. (1988) 89–96.
[3] M.K. Meyer, G.L. Hofman, S.L. Hayes, C.R. Clark, T.C. Wiencek, R.V. Strain, K.-H. Kim, J. Nucl. Mater. 304 (2002) 221–236.
[4] A. Leenaers, S. Van den Berghe, E. Koonen, C. Jarousse, F. Huet, M. Trotabas, M. Boyard, S. Guillot, L. Sannen, M. Verwerft, J. Nucl. Mater. 335 (2004) 39–47.
[5] F. Huet, J. Noirot, V. Marelle, S. Dubois, P. Boulcourt, P. Sacristan, S. Naury, P. Lemoine, Proceedings of the 9th International Meeting on Research Reactor Fuel Management (RRFM), Budapest (Hungary), 2005, pp. 88–93.
[6] S. Van den Berghe, W. Van Renterghem, A. Leenaers, J. Nucl. Mater. 375 (2008) 340–346.
[7] G.L. Hofman, Y.S. Kim, H.J. Ryu, J. Rest, D.M. Wachs, M.R. Finlay, Proceedings of RRFM 2006, Sofia, Bulgaria, March, 2006.
[8] Y.S. Kim, G.L. Hofman, A.B. Robinson, Proceedings of RRFM 2009, Vienna, Austria, March, 2009.
[9] M. Ripert, V. Marelle, X. Iltis, H. Palancher, Ch. Valot, F. Charollais, M.-C. Anselmet, X. Tiratay, P. Lemoine, S. Van den Berghe, A. Leenaers, C. Jarousse, Proceedings of RRFM 2011, Roma, Italy, March, 2011.
[10] D.D. Keiser, Y.-F. Yue, B. Yao, E. Perez, Y.H. Sohn, C.R. Clark, J. Nucl. Mater. 412 (2011) 90–99.
[11] D.D. Keiser, J. Gan, J.F. Jue, B.D. Miller, C.R. Clark, Mater. Character. 61 (2010) 1157–1166.
[12] T.B. Massalski, Binary Alloy Phase Diagrams, 2nd Ed., ASM International, 1990.
[13] M. Ripert, S. Dubois, J. Noirot, P. Boulcourt, P. Lemoine, S. Van den Berghe, A. Leenears, A. Röhrmoser, W. Petry, C. Jarousse, Proceedings of the 12th International Meeting on Research Reactor Fuel Management, Hamburg, Germany, 2008.
[14] M. Ripert, F. Charallais, M.C. Anselmet, X. Tiratay, P. Lemoine, J.G. Stevens, Proceedings of RERTR 2009, Beijing, China, November 1–5, 2009.
[15] A. Leenaers, S. Van den Berghe, W. Van Renterghem, F. Charollais, P. Lemoine, C. Jarousse, A. Röhrmoser, W. Petry, J. Nucl. Mater. 412 (2011) 41–52.
[16] E. Koonen, H. Guyon, P. Lemoine, C. Jarousse, D.M. Wachs, J.G. Stevens, Proceedings of RERTR 2009, Beijing, China, November 1–5, 2009.
[17] X. Iltis, F. Charollais, M.C. Anselmet, P. Lemoine, A. Leenaers, S. Van den Berghe, E. Koonen, C. Jarousse, D. Geslin, F. Frery, H. Guyon, RERTR 2010, Lisbon, Portugal, October 10–14, 2010.
[18] B. Kapusta, C. Sainte-Catherine, X. Averty, M. Scibetta, G.M. Decroix, M. Rommens, Proceedings of the 9th IGORR Conference, Sydney, Australia, March 24–28, 2003.
[19] M. Wintergerst, N. Dacheux, F. Datcharry, E. Herms, B. Kapusta, J. Nucl. Mater. 393 (2009) 369–380.
[20] H. Palancher, Ph Martin, V. Nassif, R. Tucoulou, O. Proux, J.L. Hazemann, O. Tougait, E. Lahéra, F. Mazaudier, C. Valot, S. Dubois, J. Appl. Crystallogr. 40 (2007) 1064–1071.
[21] H. Hammersley, www.esrf.fr/computing/scientific/fit2d, 1999.
[22] H.M. Rietveld, Acta Crystallogr. 22 (1967) 151–152.
[23] J. Rodriguez-Carvajal, 1990, FULLPROF, Version 4.40, ILL, Grenoble, France, http://www.ill.eu/sites/fullprof.
[24] J.M. Park, H.J. Ryu, K.H. Kim, D.B. Lee, Y.S. Lee, J.S. Lee, B.S. Seong, C.K. Kim, M. Cornen, J. Nucl. Mater. 397 (2010) 27–30.
[25] A. Bonnin, H. Palancher, V. Honkimäki, R. Tucoulou, Y. Calzavara, C.V. Colin, J-F. Bérar, N. Boudet, H. Rouquette, J. Raynal, C. Valot, J. Rodriguez-Carvajal, Zeit. Krist. Proc. 1 (2011) 29–34.
[26] A. Bonnin, H. Palancher, F. Charollais, M.C. Anselmet, V. Honkimäki, P. Lemoine, Proceedings of the 15th RRFM, Rome, Italy, March 20–24, 2011.
[27] K. Tangri, G.I. Williams, J. Nucl. Mater. 2 (1961) 226–233.
[28] A.E. Dwight, J. Nucl. Mater. 2 (1960) 81–89.
[29] A. Bonnin, H. Palancher, P. Cloetens, H. Suhonnen, V. Honkimäki, J. Appl. Crystallogr., private communication.
[30] A.E. Dwight, ANL 82-14 report, September 1982.
[31] X. Iltis, CEA internal report NT LCU 09-020.
[32] J. Allenou, X. Iltis, CEA internal report NT LCU 08-010.
[33] R. Jungwirth, personal communication, 2011.
[34] E. Welcomme, H. Palancher, C. Sabathier, Ph. Martin, J. Allenou, C. Valot, F. Charollais, M.C. Anselmet, R. Jungwirth, W. Petry, L. Beck, C. Jarousse, R. Tucoulou, P. Lemoine, Proceedings of RRFM 2009, Vienna, Austria, 2009.
[35] R. Jungwirth, W. Petry, A. Röhrmoser, J. Allenou, X. Iltis, RERTR 2010, Lisbon, Portugal, October 10–14, 2010.
[36] M. Nasaki, H. Tagawara, J. Nucl. Mater. 57 (1975) 187–192.
[37] H. Palancher, R. Tucoulou, P. Bleuet, A. Bonnin, E. Welcomme, P. Cloetens, J. Appl. Crystallogr. 44 (2011) 1111–1119.
[38] J. Allenou, H. Palancher, X. Iltis, M. Cornen, O. Tougait, R. Tucoulou, E. Welcomme, Ph. Martin, C. Valot, F. Charollais, M.C. Anselmet, P. Lemoine, J. Nucl. Mater. 399 (2010) 189–199.
[39] J. Gan, D.D. Keiser Jr., B.D. Miller, D.M. Wachs, T.R. Allen, M. Kirk, J. Rest, J. Nucl. Mater. 411 (2011) 174–180.
[40] S. Van den Berghe, A. Leeaners, E. Koonen, L. Sannen, Proceedings of the 12th International Conference on Modern Materials and Technologies (CIMTEC), Montecatini Terme (Italy), 2010.
[41] H.J. Ryu, J.S. Park, J.M. Park, C.K. Kim, Nucl. Eng. Tech. 43 (2010) 159–166.
[42] S. Van den Berghe, Y. Parthoen, A. Leenaers, E. Koonen, F. Charollais, P. Lemoine, Y. Calzavara, H. Guyon, Proceedings of RERTR 2011, Santiago, Chile, October 23–27, 2011.
[43] H. Palancher, N. Wieschalla, P. Martin, R. Tucoulou, C. Sabathier, W. Petry, J.-F. Berar, C. Valot, S. Dubois, J. Nucl. Mater. 385 (2009) 449–455.
[44] R. Jungwirth, H. Breitkreutz, W. Petry, A. Röhrmoser, W. Schmid, H. Palancher, C. Bertrand-Dira, C. Sabathier, X. Iltis, N. Tarisien, C. Jarousse, Proceedings of RERTR 2009, Beijing, China, November 1–5, 2009.